Journal of Alloys and Compounds 1033 (2025) 180516

Contents lists available at ScienceDirect

Journal of Alloys and Compounds

journal homepage: www.elsevier.com/locate/jalcom

Research article

Influence of microstructure refinement on co-plasticity in an Mg-4.7Al-2.9Ca alloy

Lukas Berners [a,*], Pei-Ling Sun [a], Adrian Mikitisin [b], Joachim Mayer [b], Sandra Korte-Kerzel [a]

[a] Institute for Physical Metallurgy and Materials Physics, RWTH Aachen University, Kopernikusstr. 14, Aachen, 52074, Germany
[b] Central Facility for Electron Microscopy, RWTH Aachen University, Ahornstr. 55, Aachen, 52074, Germany

ARTICLE INFO

Dataset link: 10.5281/zenodo.15142966, 10.5281/zenodo.15144219

Keywords:
Magnesium alloy
Microstructure design
Damage detection
Mechanical properties
Co-plasticity
SEM
TEM

ABSTRACT

Mg-Al-Ca alloys, composed of a soft Mg matrix and hard and brittle Laves phases, are suitable for applications at elevated temperatures. Unfortunately, the reinforcing skeleton is brittle and leads to premature failure due to cracking and decohesion from the matrix. In the present study, we achieve a largely self-similar reduction in microstructural length scale by increasing the cooling rate of an as-cast Mg-4.7Al-2.9Ca alloy. We observe this refinement mostly in terms of intermetallic strut spacing and width reduction, while the present intermetallic phase is determined to be C36. Upon refinement, the microstructures exhibit increasing compressive ultimate stress and yield stress from 96±4 MPa and 223±4 MPa at the coarsest microstructure to 117±2 MPa and 244±2 MPa at the finest microstructure. In addition, microstructure refinement leads to a change in governing damage mechanisms, which we quantified by means of both automated and manual analysis of large area scanning electron micrographs. Brittle cracking of the intermetallic skeleton dominates by a factor of 10 over the occurrence of decohesion at the Mg/intermetallic interface and both are reduced with decreasing microstructural length scale. This is accompanied by an increase of plastic slip transmission in the Laves phase from 50 to 250 slip events per 0.2 mm^2, which goes alongside a reduction of the brittle phase from 290 to 33 per 0.2 mm^2. We therefore propose that refinement of the microstructure may be used as an additional design parameter to manipulate the deformability of skeleton-reinforced Mg-Al-Ca alloys.

1. Introduction

The interest in Mg alloys as a lightweight structural material has increased in the last three decades [1]. Both, Mg alloys for high formability sheet metals and Mg alloy for use at elevated temperatures have been largely designed by the addition of expensive and environmentally harmful produced rare-earth elements (REs) to Mg alloys [2]. To overcome the usage of these REs, Mg alloys based on other elements, such as Zn, Al, and Ca have been developed showing great creep resistance [3–10] due to the presence of secondary intermetallic phases.

Various compositions in the Mg-Al-Ca system have been synthesised and analysed focusing on mechanical testing at the time-scale of creep [3,11,12] or size-scale of nano- and micrometres [13–15]. Only few focus on tensile or compressive testing at intermediate strain rates at elevated temperatures [5,16–18]. All of these studies have synthesised Mg-Al-Ca alloys showing a dual phase microstructure of primary Mg matrix and secondary intermetallic Laves phases of either cubic C15 or hexagonal C14 and C36 type. These studies have shown, that the microstructural features which govern the behaviour upon loading are phase fraction, interconnectivity and type of the Laves phase [3,18]. The latter two are considered as the main reason for the aforementioned increased creep resistance [4,9]. These features can be designed based on chemical composition but with this design strategy, higher strength is mostly accompanied by a lower elongation to fracture [18]. Therefore, it is desirable to synthesise Mg-Al-Ca alloys with microstructural features that lead to higher elongations to failure while maintaining high strengths simultaneously. This can be achieved by influencing the co-deformation behaviour between the two constituent phases during external loading. It has been shown that this co-deformation can occur by cracking of the Laves phase, shear of the Laves phase by dislocations, or decohesion of the matrix from the Laves phase [18,19]. Medghalchi and Zubair et al. [18,20] have performed a statistical study of the damage mechanisms in a bulk cast Mg-Al-Ca alloy and showed that the dominant mechanism changes with a slower strain rate leading to reduced cracking of the Laves phase. Building on this possibility to shift the balance between damage mechanisms, with the aim of designing stronger and more ductile alloys for elevated temperatures, it is desirable to achieve co-deformation that prevents fracture of the brittle phase or opening of voids at the interfaces and instead shifts co-deformation towards slip transmission to

* Corresponding author.
E-mail address: berners@imm.rwth-aachen.de (L. Berners).

https://doi.org/10.1016/j.jallcom.2025.180516
Received 16 January 2025; Received in revised form 7 April 2025; Accepted 18 April 2025
Available online 22 May 2025

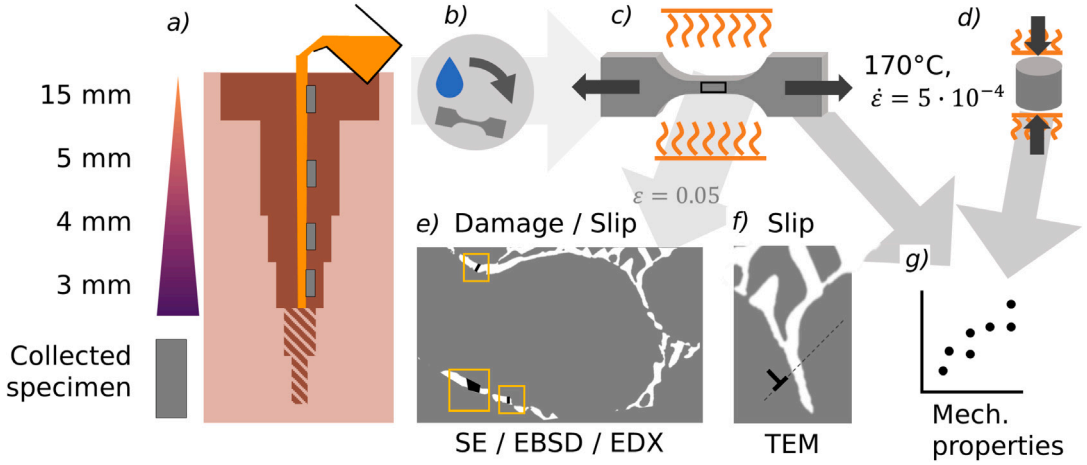

Fig. 1. Experimental setup: *(a)* Samples cast in Ar atmosphere in a copper mould, *(b)* Metallographic preparation, *(c)* Tensile testing at 170 °C and a strain rate of 5×10^{-4} s^{-1}, *(d)* Compressive testing at 170 °C and a strain rate of 5×10^{-4} s^{-1}, *(e)* Analysis of damage and slip in tensile tested samples (SEM), *(f)* Slip transmission mechanism at a dedicated site (TEM), *(g)* Evaluation of mechanical properties.

accommodate strain at high local stresses but avoid damage formation. A promising design route for achieving this is changing the microstructure [4,19–21]. Easier slip transmission can be achieved by optimising the orientation relationship between Mg and the Laves phase [7,22,23]. To achieve bulk structuring of the underlying preferred interfaces, their thermodynamic stability, the kinetics of their formation, and how this may be affected by alloying and solidification conditions must be known. However, while individual metal-intermetallic interfaces have been studied [5,24], the design and process parameters required to control different orientation relationships in Mg-Al-Ca alloys remain unknown. Here, we will therefore focus on first altering the size of the microstructural features by changing the cooling rate [3,15,25,26] based on variation of mould thickness. Other approaches of modification and refinement of the dual phase Mg-Laves phase microstructure also include more complex, cooling-rate based approaches such as melt-spinning [27] or squeeze-casting [6]. Further, mechanical processing, such as extrusion [28–31] and friction stir processing [32], or certain alloy additions such as Sr [33] and variation in Ca content [9,17,33] are used. However, all of these methods either result in a non self-similar microstructure or may change the activation of slip systems [34,35].

This study As has been pointed out above, the higher creep strength of Mg-Al-Ca compared to e.g. Mg-Al-Zn alloys has been mainly attributed to the formation of an interconnected skeleton. While it has been shown that an increase of interconnectivity is possible by means of alloying [3,18] or increase of cooling rate [3], the change of governing co-deformation mechanisms upon such a change has not been investigated. There exist only a few studies about the influence of cooling rate on the microstructural and mechanical properties of the Mg-Al-Ca alloys and to the authors' best knowledge, no study has yet tried to couple them with the analysis of co-deformation mechanisms. Therefore, this study aims to show the influence of strut width and distance, as well as interconnectivity and phase fraction of the Laves phase skeleton produced by varying cooling rates on the co-deformation between Mg matrix and Laves phase. This will lead to deriving design criteria for wall thicknesses of as-cast Mg-Al-Ca alloys. To achieve this, we will investigate the mechanical properties of the differently scaled microstructures using compression and tensile testing and correlate them to the co-deformation behaviour between the Mg matrix and the Laves phase. We will thereby statistically analyse the damage occurring inside the Laves phase network and the slip transferred from Mg matrix to the Laves phase in dedicated samples based on large-scale panoramic SEM images.

2. Experimental methods

The material used in this study was prepared from the raw materials Mg 99.9%, Al 99.7% and Ca 99.5% (purity), which were weighed to a composition of 4.7 wt −% Al and 2.93 wt −% Ca and subsequently heated in a steel crucible in an induction furnace under vacuum. Once the material melted, the atmosphere was regulated to 100 mbar Ar and the melt was poured into a stepped copper mould (confine Fig. 1) and cooled to room temperature.

From this, 8 samples have been prepared for tension and compression testing from each step between 3 mm and 15 mm, respectively (see again Fig. 1(a)). Additionally, one sample per step was used for analysis of damage in tension geometry and one sample in the 15 mm and 3 mm step for analysis of slip events. Four further samples from the 15 mm and 3 mm steps were used for a porosity analysis in an XRM device.

Both, tensile and compressive specimens were cut using wire-electrical discharge machining (EDM) at positions left and right of the central part, to exclude the influence of possible turbulences caused by the pouring stream. The resulting tensile specimens had a dog bone shape with a gauge length of 5 mm. The compression samples were cylindrical, measuring 4.5 mm in height and 3 mm in diameter.

Tensile specimens for metallographic analysis were ground using grit 2000 and grit 4000 SiC paper (Struers, ethanol as lubricant) and polished using polycrystalline diamond suspensions with grain sizes of 3 µm and 1 µm supplying ethanol and polyethylene glycol 400 as lubricant. The samples for damage analysis have been electro-polished using the Struers electrolyte AC-2 at 15 V and −20 °C for 90 s to remove remaining deformation layers followed by 1 min of oxidal polishing suspension (OPS) (Struers) polishing to remove remaining topography of the sample. To remove OPS particles, the sample was cleaned using water for 2 s followed by isopropyl alcohol cleaning for 1 min.

Mechanical testing in this study has been performed by tensile and compressive testing (schematics in Fig. 1(a) and (b)).

The samples in this study are tested on a DZM tensile device using a 12.5 kN load cell and were heated to a temperature of 170 °C.

For testing of mechanical properties, the samples were strained until fracture with a strain rate of 5×10^{-4} while for the damage analysis, the samples were only strained to 5 % engineering strain.

For compressive testing, a Zwick 1484 was equipped with a 200kN load cell. The experiment was also conducted at 170 °C with a loading rate of 5×10^{-4} in analogy to the tensile tests. The experiment was stopped, once the true stress dropped about 15 MPa below the maximum true stress.

For metallographic analysis, a Zeiss LEO 1530 was used at a Voltage of 10 kV for SE images. For EDS measurements, an FEI Helios 630 i

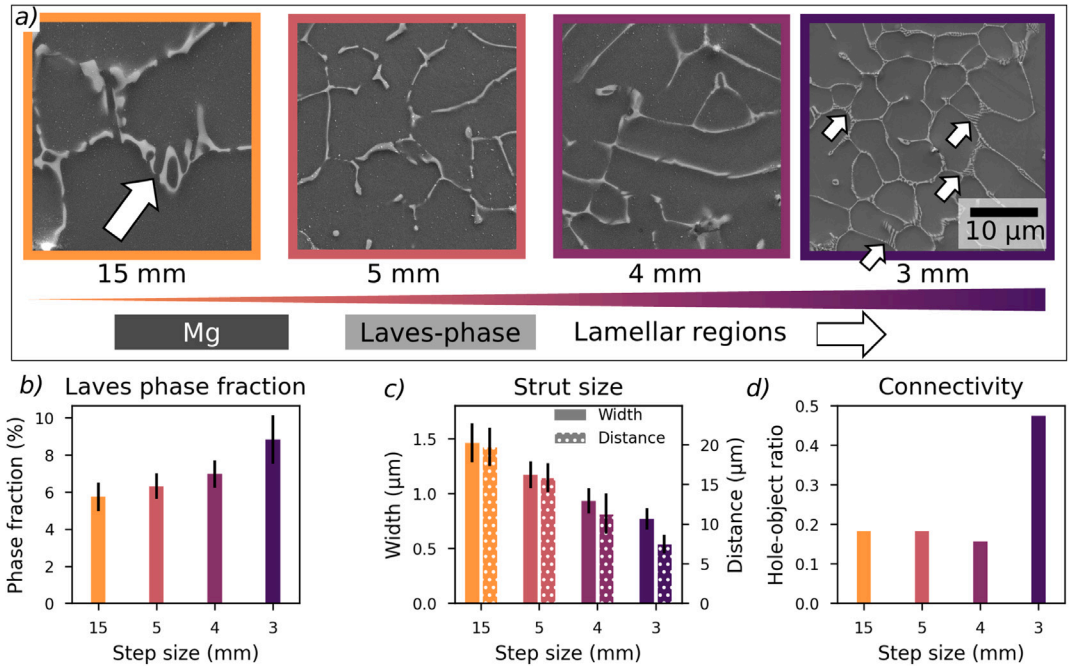

Fig. 2. Microstructures and their features in dependence of step size. From left to right the step size decreases from 15 mm to 3 mm, corresponding to an increase in cooling rate: *(a)* SEM images of the microstructure (SE contrast). *(b)* Intermetallic phase (area) fraction *(c)* Size of the intermetallic struts and distance of the struts. The dotted bars show the distance (right y-axis). *(d)* Connectivity of the microstructure represented by the ratio of holes over objects.

equipped with an Octane Super A EDS detector (EDAX Team for analysis) was used at a voltage of 10 kV, respectively. For the microstructure and damage analysis, panoramic regions of at least 500 µm × 350 µm, composed of individual images with a width of 50 µm and a resolution of 3072 × 2048 px have been recorded automatised in the SEM and stitched using image composite editor. Damage sites have been detected by a YOLOv5 [36] neural network trained for damage detection on a Mg-4.65Al-2.82Ca alloy, with the same weights as in [20]. As the performance of the network is better suited for smaller images, the large panoramics have been resampled into subsets of 4000 px × 4000 px each. For the slip site analysis, the images had a width of 25 µm and the regions were at least 400 µm × 250 µm, slip sites were then manually labelled on resampled images of 4000 px edge length using labelImg. It was ensured, that the panoramic images utilised for damage detection contained at least 20 large Mg grains of varying orientation, to rule out orientation dependent influences on our analysis.

To analyse the width of struts and phase fraction on stitched panoramic images, the same script as in [5] was used. This script performs automatic multi-otsu [37] segmentation and line sectioning of the microstructure based on ten horizontal and vertical lines. For analysis of these parameters, the same images as for damage analysis are used and the results are averaged for all images of each step. To quantify the connectivity of the microstructure, we determine the ratio of objects to holes in the analysed, stitched image. Here, we obtain the number of holes and objects, using the label and euler-number functions from the scikit-image library [37]. The holes and objects are the Mg matrix and the Laves phase respectively. These operations are performed on the stitched images used for damage analysis.

XRM analysis of dedicated tensile specimens was performed using a ZEISS Xradia 620 Versa microscope. The experimental setup allowed for the simultaneous imaging of four samples within the same field of view (FOV). A full 360-degree rotation scan was conducted, capturing a total of 1601 projections. The imaging was performed at an X-ray energy of 80 kV and a power of 10 W. A spatial resolution of 6 µm with an exposure time of 4 s per projection was used.

To obtain the amounts of oxides and pores, a median filter was applied to the image stacks, to reduce noisy segmentation of the data. Pores and oxide regions are segmented using manual thresholds of 8 % and 92 % brightness, respectively. The thus obtained binary masks have been convoluted with a binary structure kernel (see S.2 for details), to filter remaining noise. The pore density is determined based on the summed image of voxels in z direction, which makes it easy to automatically determine the boundary of the tensile specimens using a contour finding algorithm [37,38]. The maximum pore size per cross-section is based on the column-wise sum in the side view image (see again subsection S.2 for more details).

The region of interest in the sample was prepared by a dual beam (focused ion beam (FIB)-SEM) with a field emission gun (FEI Helios 630i). A thin platinum layer was deposited on the sample surface before FIB thinning to minimise the ion beam damage. A Ga^+ ion beam with a voltage of 30 kV was initially utilised to mill the sample surface and a wide trench around the area of interest, which was successively removed with smaller beam currents starting from 21 nA down to 80 pA. For the final cleaning step, a voltage of 5 kV was employed. The lamella was examined in a Jeol JEM F200 TEM at 200 kV. The device was operated in both, conventional and HR mode to obtain the images in this publication. SAED was used at different tilt angles for orientation relationship analysis of the Laves phase and the Mg matrix.

3. Results

3.1. Microstructure of the alloys

3.1.1. Micrographs of the microstructure

Examples of typical microstructures, depending on the width of the stepped mould are shown in Fig. 2. The microstructure comprises a Mg matrix (dark) and a skeleton of Laves phases (bright). A correlation between mould size, associated with an increase in cooling rate for smaller steps, and the refinement of the struts can be observed in Fig. 2. The 3 mm step leads to formation of fine lamellar regions (marked with white arrows). In contrast, lamellar regions forming at larger steps, e.g. 15 mm are coarser and appear less frequently.

Analysis of phase fraction, size of the skeleton and connectivity reveals, that an increase in cooling rate, leads to the following changes in the microstructure:

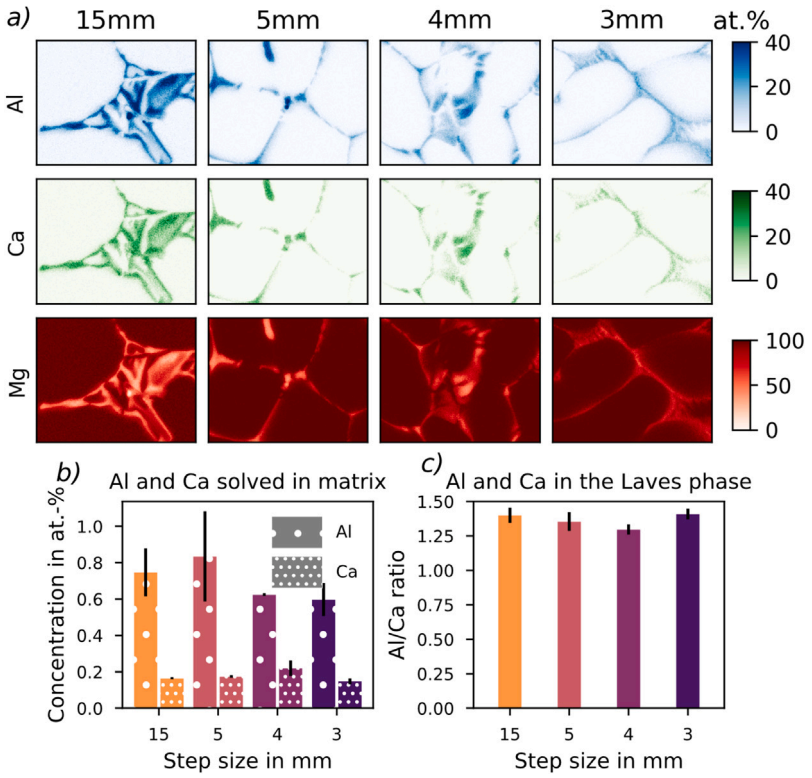

Fig. 3. Results of the EDS analysis: *(a)* EDS mappings showing the distribution of elements in the sample. A darker colour corresponds to high at. – % of each element. *(b)* concentration of Al and Ca in the Matrix, in at. – % average over multiple point measurements. *(c)* ratio of Al to Ca inside the Laves phase. (For interpretation of the references to colour in this figure legend, the reader is referred to the web version of this article.)

1. The phase fraction of the intermetallic phase increases from 5.8±0.7 % to 8.8±1 % (Fig. 2(b)),
2. The size of the struts decreases from 1.5±0.2 µm to 0.8±0.1 µm and distance from 20± 2 µm to 7.5± 1 µm (Fig. 2(c)), and
3. The connectivity, as given by the ratio of holes (Mg cells) to objects (Laves struts) increases from 0.2 to 0.5. (Fig. 2(d)).

3.1.2. EDS

The chemical composition of the different steps by EDS is shown in Fig. 3. Mappings (*(a)*) are used to display the distribution of elements in the different phases, while spot measurements (*(b)* and *(c)*) are used for quantification. From the EDS mappings, depicting the composition of Al (blue), Ca (green) and Mg (red) in the sample in at. – %. it is visible, that the Ca and Al content in the Laves phase are similar. The Mg content is around 50 at. – % in the Laves phase and the matrix is mainly composed of Mg. The results in Fig. 3*(b)* and *(c)* are based on the mean value of multiple point measurements.

The concentration of elements in the matrix is between 0.6 at. – % and 0.9 at. – % for Al and 0.1 at. – %-0.2 at. – % of Ca. The ratio of Al to Ca is between 1.3 and 1.4.

3.2. Mechanical properties

3.2.1. Compression tests

Fig. 4 displays the results from compression testing of the four different microstructures. We observed, that there is a strong dependence of maximum compression stress on the microstructural refinement with a strong increase of the maximum stress towards smaller strut widths and distances. The yield stress and maximum stress increase from 96±4 MPa and 223±4 MPa at 15 mm to 117±2 MPa and 244±2 MPa at 3 mm, respectively. The strain at maximum stress increases from 0.18±0.003 at 15 mm mould step size to 0.23±0.005 at 4 mm.

3.2.2. Tensile tests

The results from tensile tests with their main purpose of inducing damage are shown in Fig. 5 revealing a large scatter in terms of ultimate tensile stress (UTS) and yield stress ($\sigma_{0.2}$), indicated by the overlapping error bars in the inset figures, depicting the standard deviation. Disregarding the large scatter, there is a slight tendency of the 15 mm and 5 mm step samples to show higher UTS and uniform elongation values than the microstructures from the 4 mm and 3 mm steps. The UTS and uniform elongation (UE) decrease from 150±9 MPa and 16±5 % at 15 mm to 135±20 MPa and 9±7 % at 3 mm, respectively. The yield stress is within 83±6 MPa and 90±5 MPa with no observable tendency.

3.2.3. XRM experiments in 3 mm and 15 mm steps

Fig. 6 shows the results of XRM analysis on dedicated tensile specimens to assess porosity and its effect on achieved uniform elongation. During the analysis of the XRM data, we observed in addition to the pores (in black, Fig. 6(a)), bright features, which are presumably oxides (Fig. 6(b)). Fig. 6(c) and (d) show, that an increase of pores leads to a decrease of uniform elongation. Also, the yield stress and the ultimate tensile stress are decreased, with increasing porosity and size of pores (subsection S.3). The mechanical properties are mostly independent of the oxide formation (Figure S.4-Figure S.6) but depend strongly on the porosity. The analysis reveals an increased amount of pores in the more rapidly cooled samples alongside decreased UE, UTS and yield stress in tension.

3.3. Damage classification and deformation mechanisms

In order to evaluate whether the microstructural refinement influences damage formation, we investigate the amount and type of damage occurring upon deformation of samples from the different step sizes. To this end, we apply the YOLOv5 network as trained by Medghalchi et al. [20] to detect and classify damage sites.

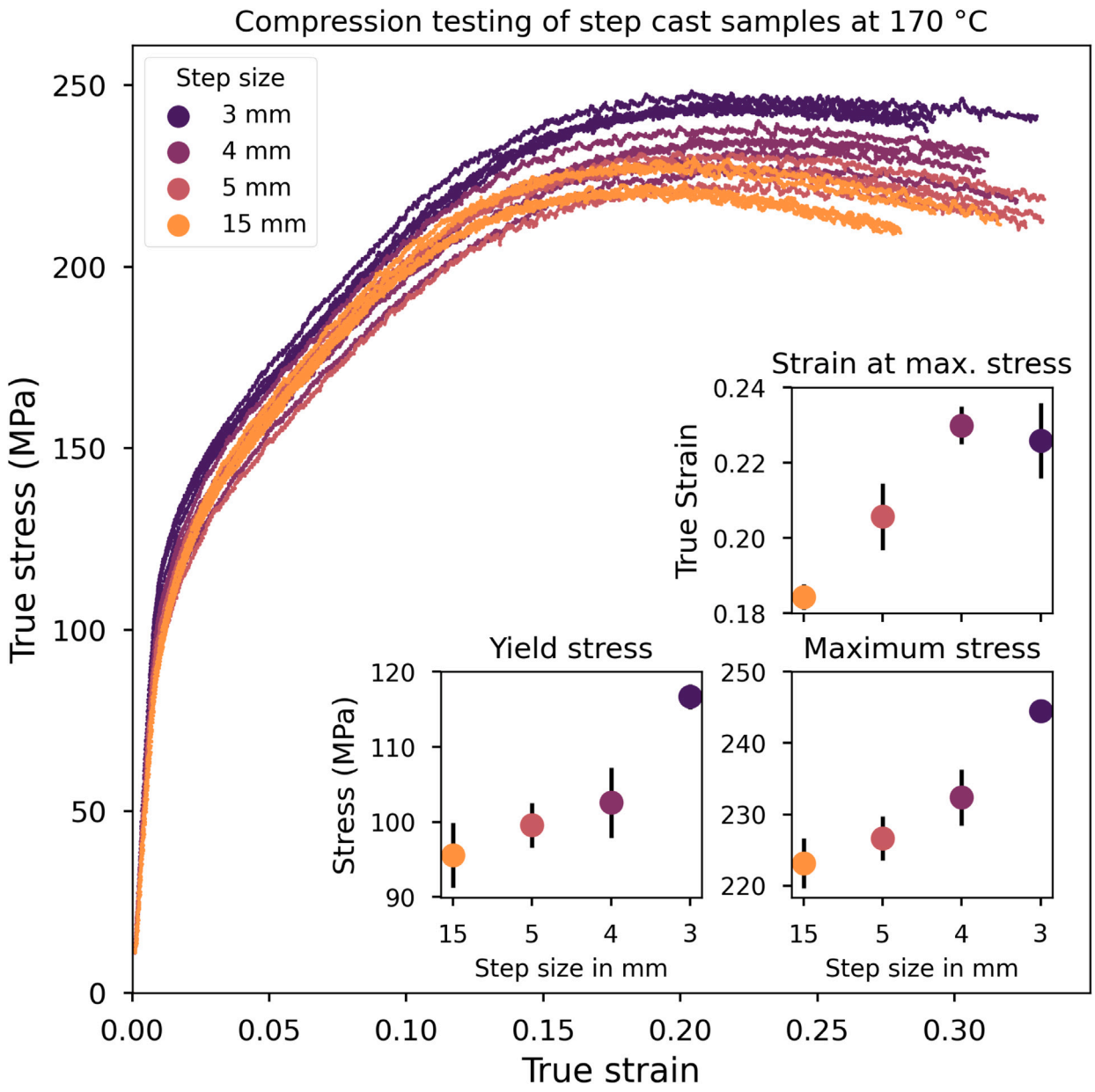

Fig. 4. True stress–strain curves from compression testing of the step cast samples at 170 ° C. The colour coding shows the respective steps. The insets show the yield stress, maximum stress and strain at maximum stress. See supplementary material for details of the analysis.

In Fig. 7 typical damage sites are shown with their classification according to the neural network into the two damage mechanisms decohesion of the Mg matrix from the Laves phase and cracking of the Laves phase. For all microstructures, apart from the 3 mm step, the number of decohesion sites was about an order of magnitude lower than the number of cracks. In the 3 mm sample, a large number of decohesion sites was observed. A comparison of these sites, labelled as decohesion on a sample before and after deformation, revealed that these sites are indeed pores resulting from sample preparation, that open up slightly during straining of the sample. Fig. 8 shows the results from the automated damage site classification. The results are normalised with respect to the measured area (about 0.2 mm^2 for each panoramic image) and show, that there is a decrease in the number of damage sites from 292/0.2 mm^2 Laves cracks in 15 mm to 33/0.2 mm^2 in 3 mm with increasing cooling rate. For the 15 mm to 4 mm steps, where we could quantify both Laves cracks and decohesion sites, we also note that their ratio does not change much.

3.4. Slip transmission from Mg to the laves phase

In addition to the automated analysis of damage sites by the convolutional neural network, we identified slip events in the Laves phase manually. For labelling, a slip line is defined as a line-shaped feature in the Laves phase which has a topographic contrast in the SEM and extends across the full width of the Laves phase precipitate (Fig. 9(e), cases I to III). This definition may include cracks, that have not opened yet, but as it is impossible to distinguish them from actual slip lines, they are included in the labelling (mostly case I). Steps at the interface of Mg and Laves phase are not labelled, as they most likely stem from surface steps on the Laves phase formed during solidification (Fig. 9,(e), case IV).

The labelling of the slip transmission sites had different caveats in both the 15 mm and the 3 mm microstructures. In the microstructures from the 15 mm step, more single-type slip events (case I) were observed, where it could not be ruled out that they are actually cracks

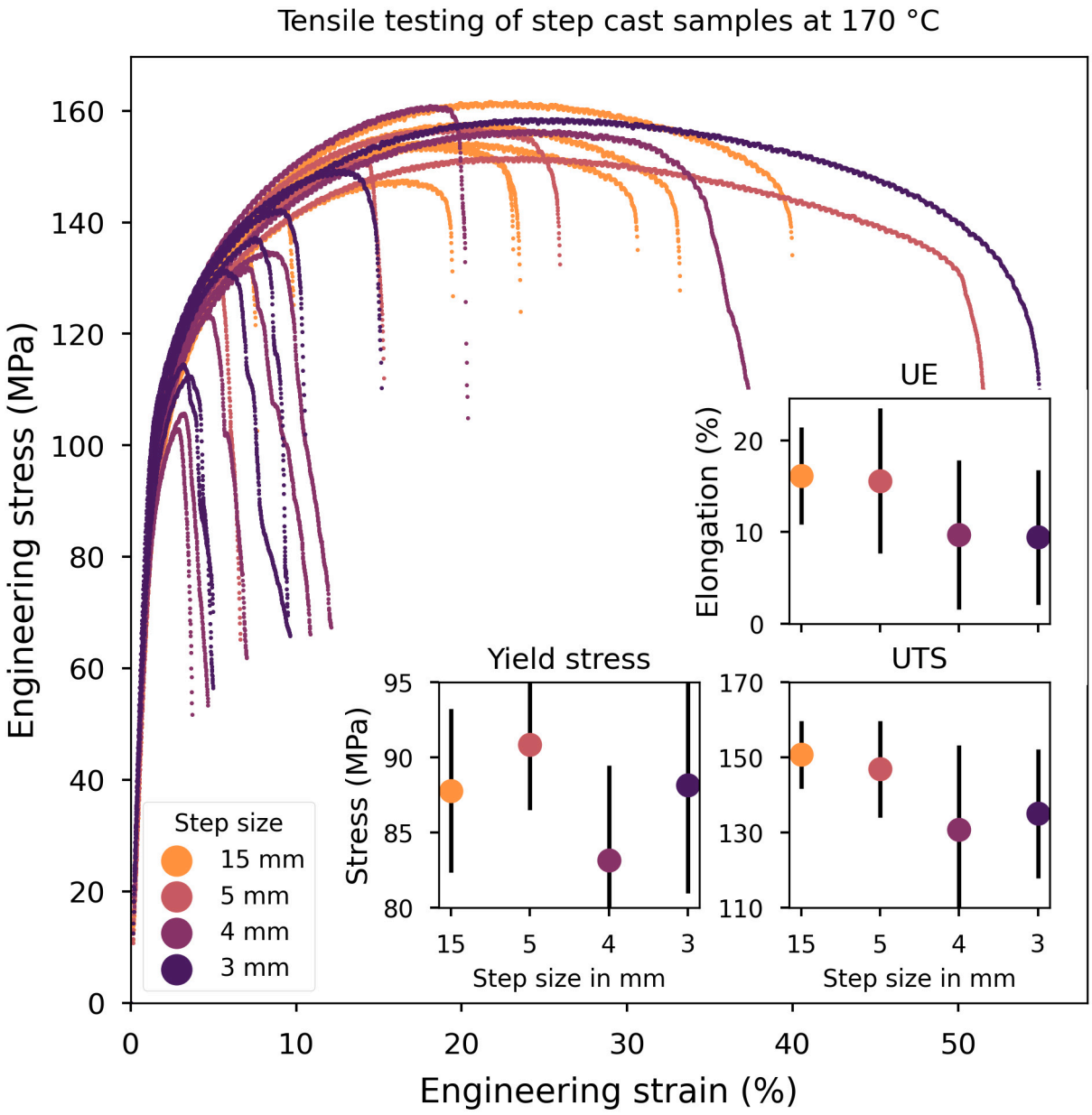

Fig. 5. Engineering stress–strain curves from tensile testing of the step cast samples at 170 °C. The insets show the mean values and scatter of uniform elongation, yield stress and ultimate tensile stress for each sample.

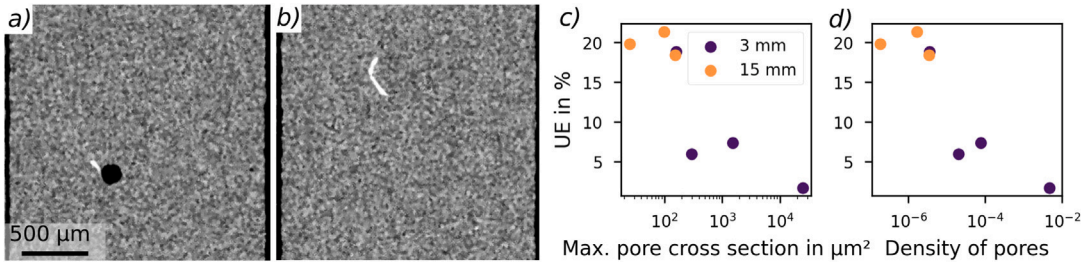

Fig. 6. Correlation between casting defects and uniform elongation: *(a)* Example of a pore from the 3 mm sample. *(b)* Example of an oxide site from a 15 mm sample, same scalebar as (a). Dependence of the uniform elongation on *(c)* the maximum pore cross-section and *(d)* on the density of pores.

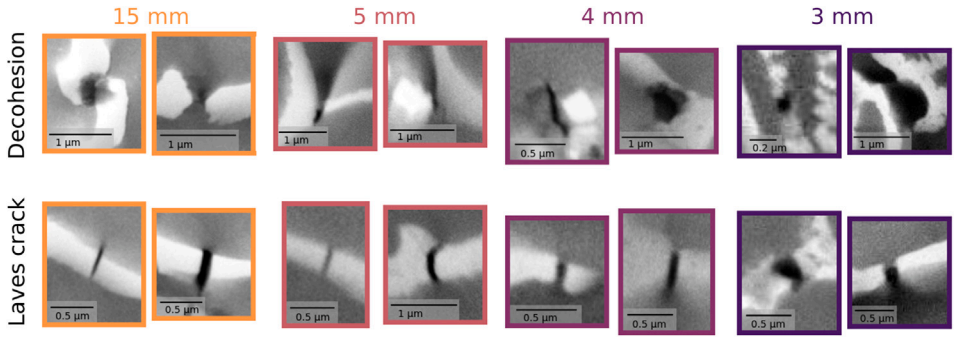

Fig. 7. Examples of damage sites (SEM images, SE contrast). The box around the images reflects the size of the machine learning label bounding box. Note that decohesion sites in the finest microstructure were partly introduced by surface preparation rather than deformation.

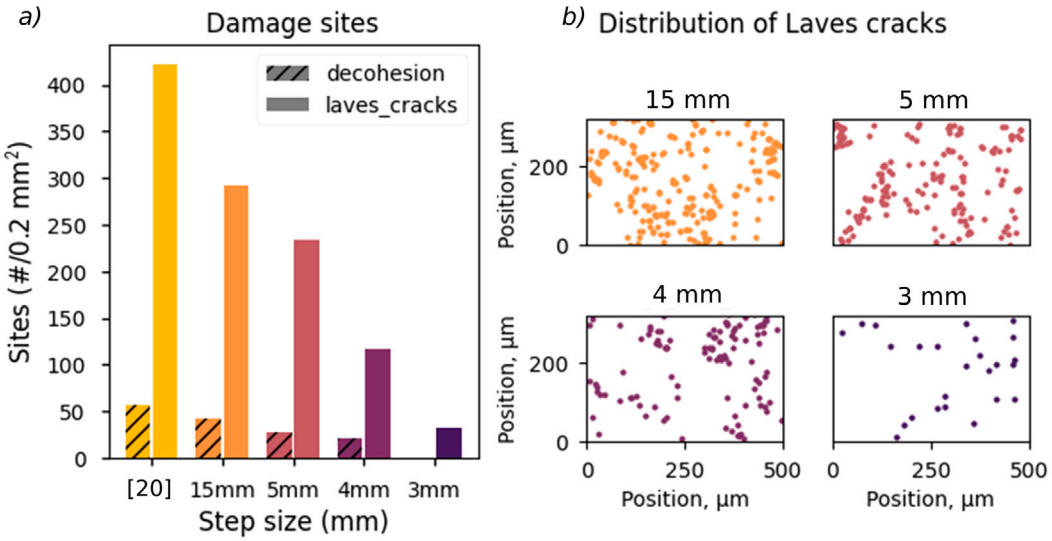

Fig. 8. Results of damage analysis: *(a)* Occurrence of cracks and decohesion sites normalised by area, the results from [20] are shown in comparison. The microstructure is expected to be coarser than the 15 mm step based on the reported cell size in [18]. *(b)* Distribution of cracks in the analysed area. Note that decohesion sites are not shown for the 3 mm step size due to the influence of surface preparation artefacts on their classification.

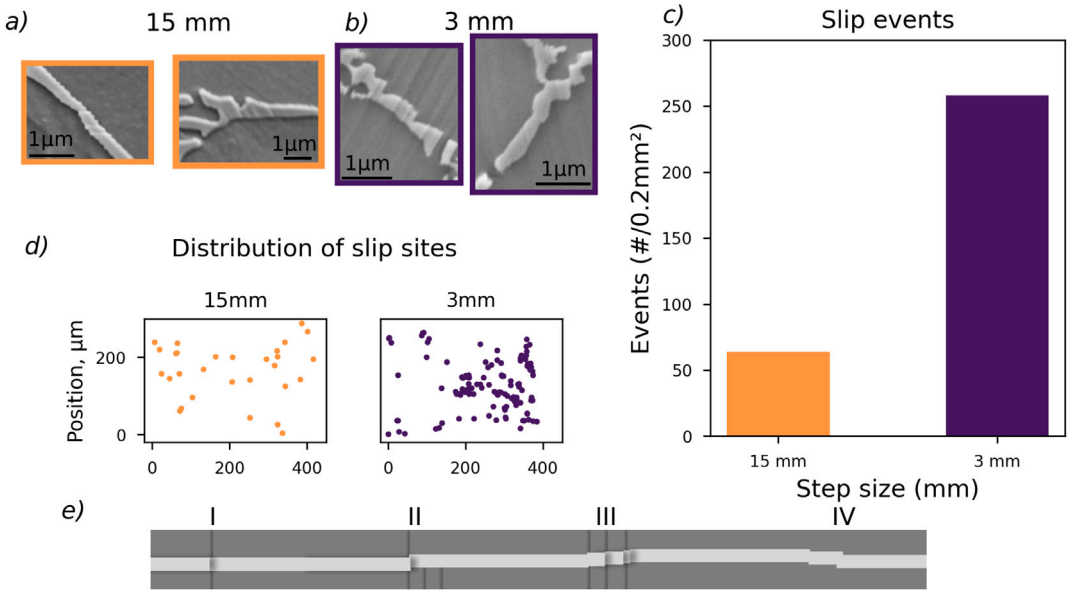

Fig. 9. : Results of manual slip detection analysis: *(a)* Slip sites from 15 mm step size microstructure, *(b)* Slip sites from 3 mm microstructure, *(c)* Occurrence of slip events normalised by area, *(d)* Distribution of slip events in the analysed area, *(e)* Sketch to explain, which contrasts in the Laves phase have been labelled.

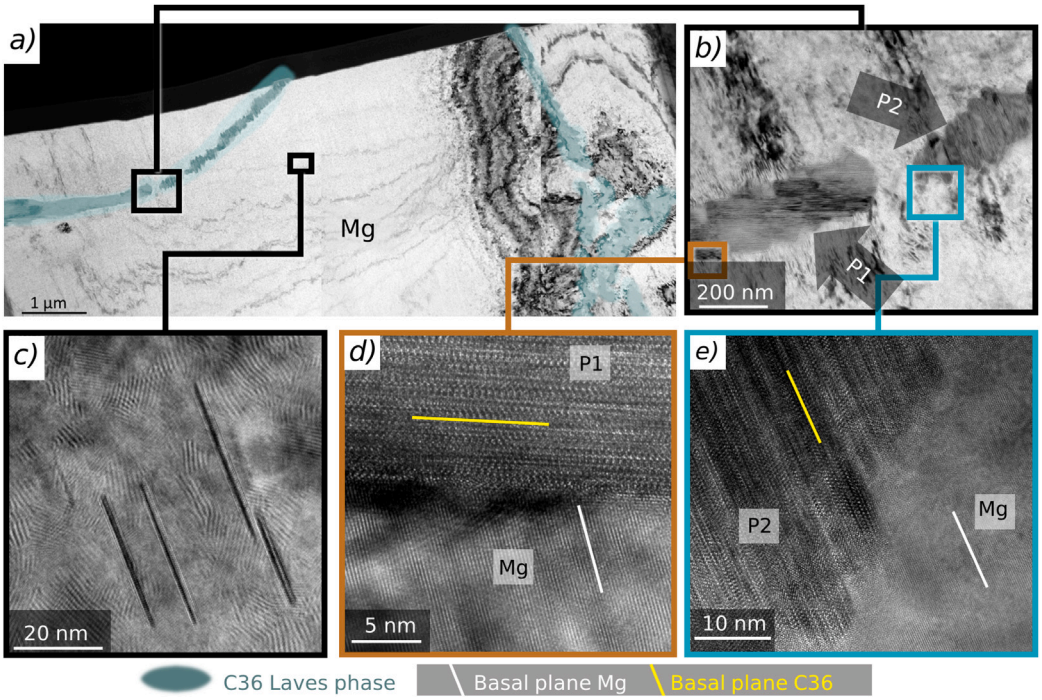

Fig. 10. Conventional and HRTEM analysis: *(a)* Overview of the lamella showing the Laves phase highlighted in blue and the surrounding Mg matrix, *(b)* Laves phase precipitates P1 and P2 inside the TEM lamella, *(c)* precipitates lying on the basal plane of Mg matrix, *(d)* P1 and Mg, and *(e)* P2 and Mg. (For interpretation of the references to colour in this figure legend, the reader is referred to the web version of this article.)

in the Laves phase. In the 3 mm microstructure, the precipitated Laves phase is not as smooth and appears to already contain many surface steps, which are not deformation-induced and therefore makes it more difficult to identify actual topographic contrast in the Laves phase in this microstructure. Additionally, the struts in the finer microstructures are more difficult to maintain in accurate focus during automatic panorama acquisition across a large area that may vary in local height as a result of deformation. However, in the supplementary material (Figure S.8), we show that slip traces can still be identified by the intensity contrast they induce, even if the image is out of focus.

The results of this manual analysis are shown in Fig. 9. The number of slip traces found in the 3 mm microstructure (258/0.2 mm^2) is much higher than for the microstructure with 15 mm mould step size (64/0.2 mm^2).

3.4.1. TEM results

We used TEM to further investigate the co-deformation by slip across the two phases. The results obtained from a TEM lamella of a slip trace in the finest microstructure (3 mm) are given in Fig. 10. The lamella was milled in such a way that it contains a surface slip trace intersection between the Mg matrix and the Laves phase precipitates. Fig. 10(a) shows the distribution of Laves phase inside the lamella, highlighted in blue. A few discrete Laves phase precipitates appear in the right side of the lamella. Three of these precipitates located close to the sample surface were analysed and two of them are found to have a similar orientation. Therefore, only the ones with different orientations (hereafter named P1 and P2) are investigated, shown by an enlarged image in Fig. 10(b). HRTEM images showing the interfaces of P1/Mg and P2/Mg are given in Fig. 10(d) and (e). The basal planes of the C36 Laves phase and Mg matrix are indicated by the yellow and white lines, respectively. The basal plane of the P1 Laves phase intersects the basal plane of the Mg matrix at an angle of 73° (Fig. 10(d), while for P2 the basal plane of the Laves phase is nearly parallel to the basal plane of the Mg matrix (Fig. 10(e).

Different zone axes of the Laves phase precipitates were reached in the TEM and compared to the theoretical data to confirm the presence of the C36 Laves phase (the SAED patterns are shown in Fig. 11(a), (c) and (e)). Additionally, the Mg matrix was tilted to different zone axes to identify the orientation relationships between P1/Mg and P2/Mg. The two precipitates were found to have different orientation relationships with the Mg matrix. For P1, the angle between $Mg_{[0\bar{1}10]}$ and $C36_{[\bar{1}\bar{1}20]}$ was determined to be 4.6°. P2 shows another orientation relationship where the angle between $Mg_{[0\bar{1}10]}$ and $C36_{[\bar{1}\bar{1}20]}$ is 2.7° (Fig. 11(c)) and (d)). Additional diffraction patterns from P2 show a deviation of 3.6° between $Mg_{[\bar{1}\bar{1}20]}$ and $C36_{[\bar{1}010]}$ (Fig. 11(e)) and (f))

In addition to the coarse precipitates P1 and P2, the Mg matrix contains fine precipitates lying on the basal plane (Fig. 10(c)), as has been reported before [19,24] in other similar alloys. The matrix itself shows a high dislocation density, and, as revealed by the two-beam conditions, both, <a> and <c+a> type dislocations are present. The Laves phase also shows a high density of dislocations but the dislocation type was not determined in this work. The C36-Mg interface appears stepped, which is also visible in SEM images. Fig. 10(d) highlights that these steps occur along the basal plane.

Both precipitates, P1 and P2, contain a high density of stacking faults, revealed in the HRTEM images in Fig. 10(d) and (e). The stacking faults give rise to long streaks along the [0001] direction in the $[\bar{1}\bar{1}20]$ SAED patterns (Fig. 11(a), (c)), while the $[\bar{1}010]$ for P2 shows no streaks (Fig. 11(e)).

4. Discussion

In this work, we aimed to study the influence of the microstructural length scale on the mechanical properties and co-deformation behaviour between the soft Mg matrix and hard Laves phase precipitates. We will discuss our results along the following research questions in detail:

1. How does the increase in cooling rate change the microstructure?
2. How do these changes in the microstructure affect the mechanical properties?

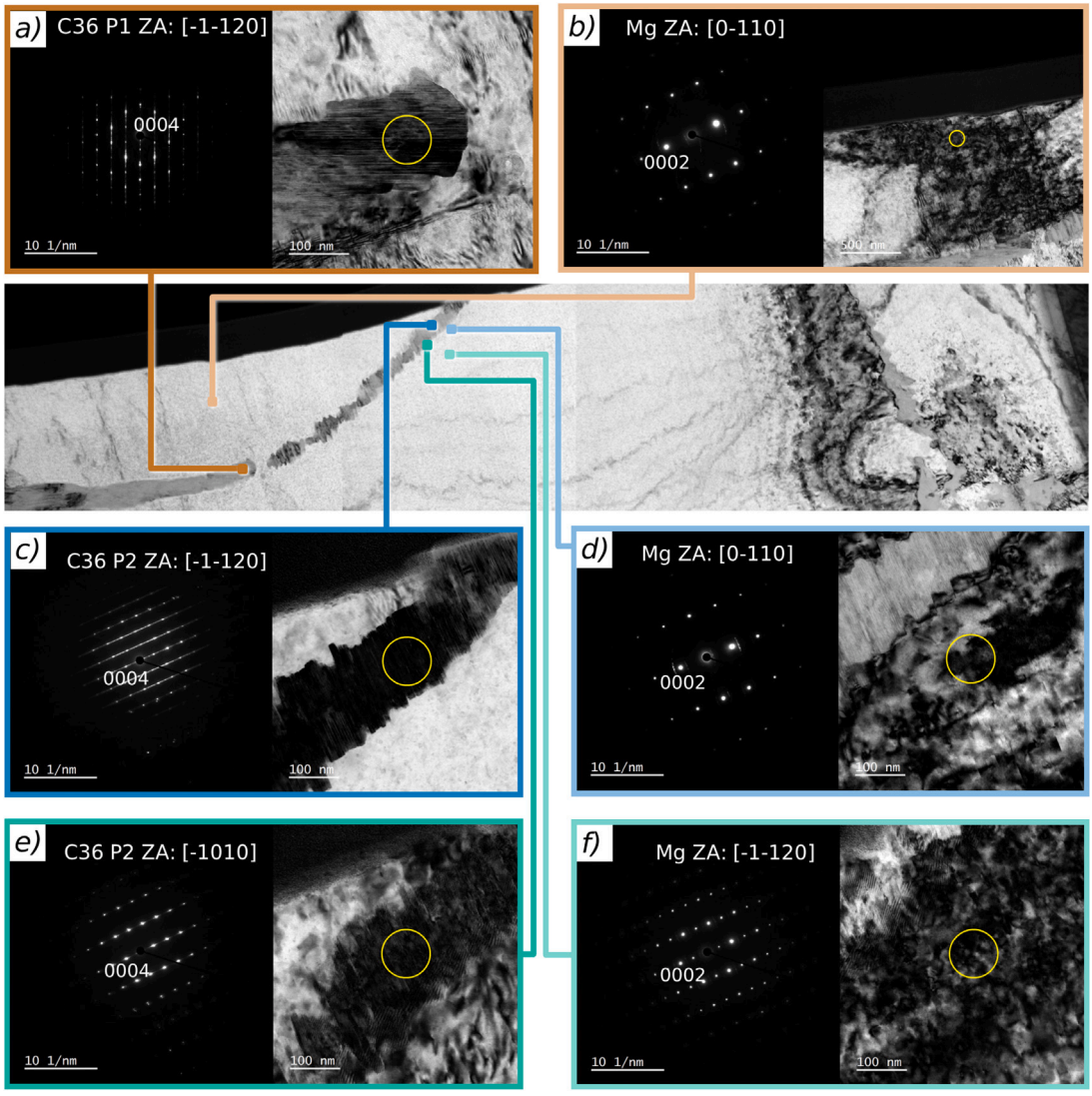

Fig. 11. TEM images and SAED patterns for orientation relationship analysis: The insets *(a)* - *(f)* show the image and the SAED patterns of the Mg matrix or the Laves phase precipitates, respectively. The diffraction area is highlighted with a yellow circle in each image. The centre location of each inset image is marked with a rounded square. *(a)* C36 Laves P1 at zone axis $[\bar{1}\,\bar{1}\,2\,0]$. *(b)* Mg matrix at zone axis [0-110]. *(c)* C36 Laves phase P2 at zone axis $[\bar{1}\,\bar{1}\,2\,0]$. *(d)* Mg matrix at zone axis [0-110]. *(e)* C36 Laves phase P2 at zone axis $[\bar{1}\,0\,1\,0]$. *(f)* Mg matrix at zone axis $[\bar{1}\,\bar{1}\,2\,0]$. (For interpretation of the references to colour in this figure legend, the reader is referred to the web version of this article.)

3. How does a difference in microstructural length scales change the co-deformation between the Mg matrix and the C36 Laves phase?
4. How do the microstructural length scales in combination with the co-deformation mechanisms translate to macroscopic mechanical properties?
5. Which implications on the design of Mg-Al-Ca alloys with an interconnected skeleton result from these insights?

4.1. Influence of the cooling rate on the microstructure

As shown in Fig. 2, the reduction in step size and therefore increase in cooling rate, influences the morphology of the microstructure in terms of a refinement of the Laves phase network, an increase of intermetallic phase fraction and connectivity of the skeleton. This is in qualitative agreement with previous studies on the present Mg-Al-Ca system [3,11,15] and other types of Mg-alloys [39].

Further, the results of the EDS analysis are in good agreement with those of previous studies in the Mg-Al-Ca system on slowly cooled alloys [18,40,41]. Amerioun et al. [40] have shown, that the co-existence range for the C36 Laves phase ($CaAl_{2-x}Mg_x$) extends between $x = 0.66$ and 1.07 (corresponding to Al/Ca ratios of 1.34 and 0.93, respectively). Consequently, the Al/Ca ratio of around 1.3–1.4 found in this work is still in the expected compositional range for the C36 Laves phase, even if there may be some influences due to excess detection from the matrix phase, as has been observed before [18,32].

Therefore, we expect the Laves phase precipitates to be of C36 type in all samples analysed. For the 3 mm step size, this is also confirmed by TEM using selected area diffraction (Fig. 10).

In addition to the aforementioned changes in phase fraction and connectivity, we have observed features that appear self-similar: In all samples, the mean grain diameter is larger by a factor of 5–10 (Figure S.1) than the mean strut distance. Therefore, the strut distance remains well below the grain size, suggesting that the grain size will have a negligible effect on dominant deformation mechanisms and mechanical properties. Similarly, the mechanisms of co-deformation are expected to be affected more strongly by the local strut width. At the same time, interconnectivity is expected to have a stronger effect on the overall mechanical properties but can be taken into account separately in its assessment.

Furthermore, several features, such as stacking faults lying on the basal plane in both Mg and the Laves phase are observed in the TEM

lamella extracted from the fast-cooled sample with the smallest step size. This indicates that both the matrix and the precipitates have a sub-structure on the nano-scale similar to other, slowly cooled as-cast samples [5,24] and thus again show self-similarity of the alloys cooled at different rates.

In summary, we find that by altering the cooling rate of the castings in this study, we have been able to successfully alter the microstructural features of the Mg-4.7Al-2.9Ca alloy towards smaller and more closely spaced struts. EDS analysis confirms that the chemical changes in the sample are rather small with a constant Al/Ca ratio achieved in the Laves phase.

The presented samples are therefore well suited to separate and elucidate the effects of microstructural length scales on overall mechanical properties and the underlying mechanisms of co-deformation of the phases and formation of damage in the composite microstructure.

4.2. Influence of microstructure on mechanical properties

We conducted compression tests to investigate the effect of microstructural changes on mechanical properties, while minimising the effect of different pore contents that strongly affect mechanical property measurements in tension.

We found an increase in the yield strength due to microstructure modification with decreasing step size. However, the microstructure modification includes the aforementioned increase in intermetallic volume fraction and interconnectivity. Both of which are expected to shift the yield strength towards higher values and therefore any effect of decreasing strut width and distance cannot be assessed directly.

The values for UTS and yield stress measured at 170 °C for the 15 mm step size in this work are about 30 MPa (20 %) higher than reported by [18], where a similar phase fraction of intermetallic (5.8 % in this study vs 6.8 % in [18]) and only slightly smaller strut sizes, based on visual comparison with the images in that study (Fig. 1 in [18]), were reported. Their sample synthesis may have led to a higher amount of porosity, giving a reduced UTS, this is supported by the generally lower uniform elongation compared to our study.

Further, the measurement of mechanical properties using tensile testing was prone to large scattering, which was attributed to casting porosity. Although deformation in tension was mainly performed to induce microstructural damage in the form of cracks and voids, it is nevertheless important to confirm the hypothesis that the scattering tendency of the data is indeed related to the amount of casting defects. To this end, we performed X-ray microscopy. As revealed by Fig. 6, we confirmed the expectation that an increase in pore size and volume fraction is detrimental to all reported mechanical properties, i.e. yield stress, UTS, and uniform elongation. There was also a trend of the more rapidly cooled samples to contain higher amounts of pores, which is consistent with reports from the literature [11]. We also found that the oxides observed during the XRM scan appeared to have no discernible influence, which may be attributed simply to their smaller overall volume fractions compared to the pores.

4.3. Co-deformation in scaled microstructures

In addition to the dependence of mechanical properties on the microstructures produced with different cooling rates, our study aims to unveil the influence of the similar microstructures on co-deformation mechanisms between the Mg matrix and the Laves phase.

4.3.1. Co-deformation by cracking and slip transmission

Previously reported co-deformation mechanisms are cracking of the brittle Laves phase, decohesion of the Mg matrix from the Laves phase skeleton and transmission of plasticity through the Laves phase by dislocation movement [19,20]. The former two lead to the formation of voids and are therefore considered damage sites that are especially relevant for failure under tensile conditions. To identify and classify these damage sites, a neural network, developed by Medghalchi et al. [20], was used in our study to identify cracks and decohesion sites. The number of approximately 290 Laves crack sites per 0.2 mm^2 found for the 15 mm step is below the 2100 mm^2 (corresponding to 420 cracks in 0.2 mm^2) found by Medghalchi et al. [20] at the same strain rate of 5×10^{-4} s^{-1} and strain of 5 %. The reason for this may be a larger distance of the struts of 32 µm as reported in [18] vs 20 µm in our case. Our analysis reveals, that increasing the cooling rate can be an effective measure to decrease the number of damage sites in the Mg-4.7Al-2.9Ca alloy.

In our analysis of slip traces in the Laves phases, we found, in agreement with the proposal by Zubair et al. [19], a smaller number of cracks and more slip intersections in the Laves phase at the 3 mm step, i.e. the much finer microstructure produced with the highest cooling rate.

An apparent explanation for the increased plasticity and decreased number of Laves phase cracks is the reduced thickness of the Laves phase [22], as the size effect on fracture in brittle materials [42] favours plasticity in small volumes of macroscopically brittle materials like the Laves phases [43,44]. The formation of steps on the interface of the precipitates in the finer microstructures with protruding basal plane segments provides another possible reason for enhanced slip transmission, as these steps may provide local nucleation sites for dislocations.

The increase in slip transmission, as opposed to fracture of the Laves phase, appears to be primarily related to the reduction in Laves phase strut thickness, which favours plastic deformation of the brittle phase.

Based on the findings from our EDS analysis (Al/Ca=1.40±0.05 for the 15 mm sample and 1.41±0.04 for the 3 mm) sample a change of the site lattice occupancies in the Laves phase leading to softening is not expected, as in the C15 phase a small addition of Mg had a small effect [45,46].

4.3.2. Slip as precursor to cracks

A mechanism frequently observed in Laves phases and other topologically-close-packed phases, is the beginning of cracks and the subsequent crack opening at slip planes [43,47]. Medghalchi et al. [20] even attributed the reorientation of cracking angle from 90° towards more inclined angles in a tensile tested Mg-4.65Al-2.82Ca alloy to the occurrence of cracks at regions of high dislocation density inside the Laves phase. This was a result of localised slip in experiments where the strain rate was reduced at constant temperature. Guenole et al. [48] performed atomistic simulations on stressed Mg/C14 $CaMg_2$ Laves composites, which also revealed a thermally activated transition from cracking to slip transmission at the point of intersection of basal slip bands in the Mg phase with a hexagonal C14 Laves phase. Therefore a competition between cracking and decohesion exists with a transition point of the prevalent mechanism between strain rates of 5×10^{-4} s^{-1} and 5×10^{-6} s^{-1} at 170 °C [20].

To investigate this further, we performed a similar analysis of crack inclination angle, as done in [20], manually (conf. Fig. 12(a)). This analysis (Fig. 12(b)) shows the preference of crack angles close to 90° to the stress direction for the 15 mm step size microstructure, although the distribution is broader than observed in [20]. The data for the 3 mm samples is sparse due to the low total number of observed cracks but still shows a preference for crack angles above 45°. The high amount of cracks perpendicular to the boundary of the Laves phase (Fig. 12(c)) renders slip as a precursor to cracking unlikely for a majority of the detected cracks. In this case, the angle would be expected to show a wider distribution due to slip lines being observed in a variety of angles to the Laves phase interface. These findings are then again also in agreement with the simulation work by Guenole et al. [48] and with the observation that overall crack density decreases with concurrent increase in slip events. If slip events would routinely act as crack precursors, the observed trend should not hold. In this case, size effect on energy released during crack growth would be counteracted by the formation of large, through-thickness flaws with a lowered surface energy in the form of slip planes with high dislocation density.

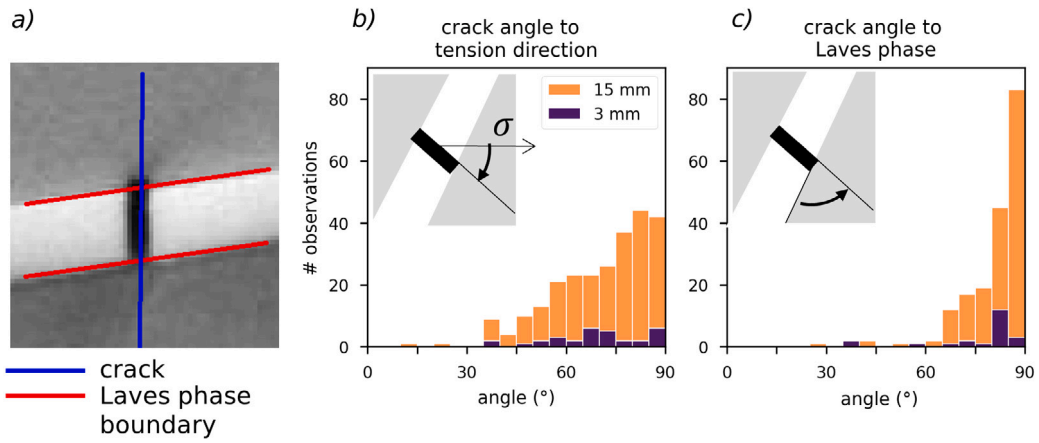

Fig. 12. *(a)* Manual inclination analysis of the cracks (in blue) and the boundary of the Laves phase (in red). *(b)* Cracking angle with respect to the tensile direction *(c)* Angle between cracks and the boundaries of the Laves phase. (For interpretation of the references to colour in this figure legend, the reader is referred to the web version of this article.)

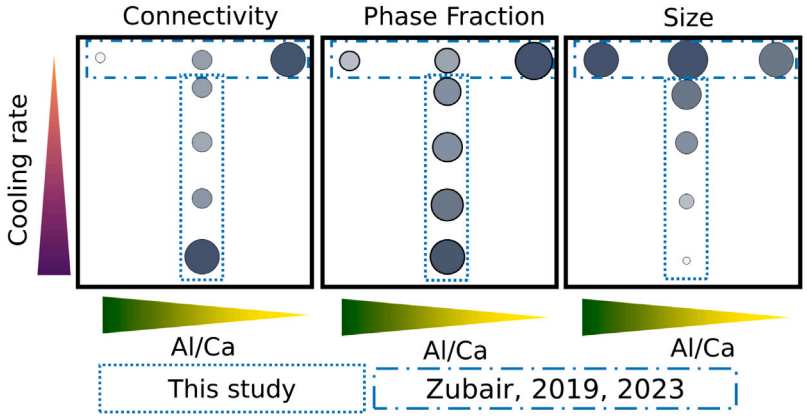

Fig. 13. Two-dimensional design space spanned by the cooling rate (size of step in copper mould) and chemistry (Al/Ca ratio). The diameter of the circles corresponds to the qualitative change of property. Blue dash-dotted lines highlight results from [5,18]. (For interpretation of the references to colour in this figure legend, the reader is referred to the web version of this article.)

4.4. Connection between microstructure, damage, co-plasticity and mechanical properties

In parallel to the decreased amount of cracks and increased amount of slip transmission events in the Laves phases with microstructural refinement, an improvement of the yield stress and maximum compression stress during compression testing was observed. As the tensile testing is heavily influenced by porosity, premature failure due to pores likely conceals any beneficial effects of the reduced Laves phase cracking. If the porosity is in the same order of magnitude for different samples (cf. Fig. 6 and Figure S.4), a similar magnitude of uniform elongation, yield stress and UTS can be achieved.

The increased cooling rate also increases the connectivity of the intermetallic struts, which was found to drastically reduce the ductility of as-cast Mg-Al-Ca alloys [18] and other material systems [49,50] due to their higher network rigidity [18,51]. Since for similar porosity densities the rapidly cooled samples have uniform elongations as high as the slowly cooled samples, we conclude that the increased slip transmission behaviour is likely to counteract negative effects of the increased connectivity and is therefore beneficial for the ductility of the alloy.

While the plasticity of the skeleton is desirable to facilitate higher deformability of the whole alloy with less damage nucleation, the hard phase still needs to shield the load applied to the material to maintain the improved creep properties this alloy was originally designed for [3, 18].

The TEM analysis of the finest microstructure (3 mm step size) shows a high density of dislocations observed near the Mg-Laves interface including <c+a> dislocations, and thus indicates the increase of stress in presence of the adjacent Laves phase. This is in analogy to other reports of back-stress hardening due to eutectic particles in Mg-alloys [19,52]. Therefore, the principal co-deformation mechanism in the present alloys is likely based on forward stresses that can nucleate dislocations in the Laves phase, as observed by Zubair et al. [19] before.

Zubair et al. [18] have shown that for increasing the network rigidity, the load-bearing capacity is increased. However, they also did report decreased ductility if the connectivity becomes too high. Similar trends for the load shielding behaviour have been observed by Amberger et al. [3] In this study, we have shown that the ductility of the alloy will be improved alongside an increased rigidity if the amount of plasticity is increased at the same time, which is possible by thinning down the struts using the cooling rate.

4.5. Further implications for alloy design

The three tunable parameters (spacing and size of the struts, amount of second phase, and connectivity of the Laves phase skeleton) can be influenced by the cooling rate, the composition [5,18] or both, therefore spanning a 2-dimensional microstructure design space. Fig. 13 displays the qualitative changes found in our study and previously by Zubair et al. [18,22]. As expected, the size of the struts is mostly influenced by the cooling rate, while connectivity and phase fraction

can be increased by both, increasing the Al/Ca or cooling rate. Additionally, the connectivity only increases significantly with the fastest analysed cooling rate in the present study. Thus, the three parameters can be tuned individually to a certain degree.

The following thoughts on alloy design are guided by the assumption, that a higher connectivity will improve the alloy creep strength [3, 18], while finer struts will increase the alloy's ductility ([19] and this study).

Producing alloys for even higher creep strengths: Amberger et al. [3] and Zubair et al. [18] have identified the connectivity of the intermetallic Laves phase as a major influence on increasing the creep strength. Tuning the connectivity by increase of the cooling rate will lead to a refined micro-structure at the same time and thus also possibly improve the ductility of the alloys at regimes of higher strain, which still may be relevant for safety of components. In contrast, the increase of connectivity by changing the Al/Ca ratio leads to more brittle behaviour, especially at higher strain rates [18]. Zubair et al. [19] showed high creep at interfaces by means of indentation. The increase of connectivity will likely also increase the interface available for mechanisms such as decohesion to act on. However, Amberger et al. [3] still observed an improved effect if the microstructure was refined.

Reducing the preliminary failure of already creep-resistant alloys: The amount of damage, especially of Laves cracks, is greatly reduced with decreasing cooling rate. Therefore, alloy compositions that have a higher connectivity than the alloy investigated in the present study (e.g. AX44 in [18]) may become more ductile during deformation at strain rate regimes faster than conventional creep (that is towards the case studied here, $5 \times 10^{-4}\,s{-}^{1}$).

Further, while increased strength of Mg-Al-Ca alloys can be achieved by, e.g., extrusion [28] or friction stir-processing [32], these processing techniques will destroy the interconnected Laves phase skeleton, which is important for creep resistance [13,19]. Therefore, the microstructural refinement may also lead to alloys that have a wider range of mechanical load cases, and may therefore be used to bridge high creep strength with damage tolerance at room temperature.

Reducing Ca-induced casting defects: As an increase in connectivity and phase fraction could be achieved by decreasing the cooling rate and decreasing the Al/Ca ratio (starting from the rapidly cooled microstructures), there likely exists a point at lower Al/Ca ratios and lower cooling rates, that has a similar phase fraction and connectivity as a point at medium Al/Ca and fast cooling rates. The resulting microstructure, will however also have a larger strut size. This approach is suitable, if for a given phase fraction and connectivity the amount of casting defects (pores) needs to be reduced and the strut size is of secondary importance.

In addition to variation of alloying elements, increasing the cooling rate is therefore a promising route for finding more ductile alloys in the Mg-Al-Ca system. Regarding the microstructures investigated in this work, the alloy from the 3 mm step showed the most promising properties, as it had the highest yield and maximum stresses under compression testing, and a heavily reduced number of cracks inside the Laves phase, although its creep performance remains to be assessed.

5. Conclusion

In the present study, we analysed the dependency of the microstructure size on cooling rate during casting of an Mg-4.7Al-2.9Ca alloy on the microstructural and mechanical properties. Furthermore, we reported insights into the change of co-deformation behaviour, as revealed by crack formation and plasticity of the skeleton in dependence on the step size. Therefore the main conclusions of this study are:

1. We successfully refined the microstructure of Mg-4.7Al-2.9Ca by increasing the cooling rate with decreasing step size. This leads to an increase in connectivity of the intermetallic skeleton and the phase fraction of Laves phase, while keeping the constituent phases the same and changing the microstructure, such that it is self-similar.
2. With decreasing step size the yield stress and compressive stress are improved from 96±4 MPa to 117±2 MPa and from 223±4 to 244±2 MPa. Further, the elongation at maximums stress increases from 0.18±0.003 to 0.23±0.005. This is connected to the refinement, increase of phase fraction and connectivity of the Laves phase skeleton.
3. The step-size-dependent refinement of the microstructure leads to a decreased amount of cracking and increased observation of slip transmission sites.
4. Cracking and slip transmission seem to be independent mechanisms and it is unlikely, that slip precedes cracking in the majority of investigated cracks.
5. Tailoring of the connectivity, intermetallic phase fraction and microstructure scale can be efficiently designed by the two dimensional space of cooling rate and alloying addition. Therefore, the investigated alloy can be optimised for higher creep resistance and reduction of preliminary failure or casting defects, such as pores.

CRediT authorship contribution statement

Lukas Berners: Writing – original draft, Visualization, Software, Methodology, Investigation, Formal analysis, Data curation, Conceptualization. **Pei-Ling Sun:** Writing – review & editing, Visualization, Investigation, Formal analysis, Data curation. **Adrian Mikitisin:** Writing – review & editing, Investigation, Formal analysis, Data curation. **Joachim Mayer:** Writing – review & editing, Funding acquisition. **Sandra Korte-Kerzel:** Writing – review & editing, Supervision, Project administration, Funding acquisition, Conceptualization.

Declaration of competing interest

The authors declare that they have no known competing financial interests or personal relationships that could have appeared to influence the work reported in this paper.

Declaration of Generative AI and AI-assisted technologies in the writing process

During the preparation of this work the author(s) used grammarly, RWTH-GPT and DeepL in order to check for spelling and grammar errors as well as language conciseness and style. These tools were not used for generation of new text but only for modification of existing text passages. Further, after using grammarly, RWTH-GPT and DeepL, the author(s) reviewed and edited the content as needed and take(s) full responsibility for the content of the published article.

Acknowledgement

This work was supported by the German research foundation (DFG) within the Collaborative Research Centre SFB 1394 "Structural and Chemical Atomic Complexity—From Defect Phase Diagrams to Materials Properties" (Project ID 409476157) including the project group C02. Analysis of damage sites and characterisation of micro-structure was performed with computing resources granted by RWTH Aachen University under project rwth-1308. The data used in this publication was managed using the research data management platform Coscine with storage space granted by the Research Data Storage (RDS) of the DFG and Ministry of Culture and Science of the State of North Rhine-Westphalia (DFG: INST222/1261-1 and MKW: 214-4.06.05.08 - 139057). We are thankful for Prof. Hauke Springer, Nadia Ayeb and Dennis Klapproth for providing the sample material (CRC 1394). Further, we want to thank Markus Felten and Jun Li for providing the code from [5] for automated strut width and distance analysis. We express our thank to Sylvester Solaiman for help with metallographic preparation and stitching of the panoramic images. We are grateful to Thomas Burlet for his technical support with mechanical testing and David Beckers for metallographic preparation. We also like to thank Maximilian Wollenweber for detailed discussions and Setareh Medghalchi for help with the YOLOv5 neural network.

Appendix A. Supplementary data

Supplementary material related to this article can be found online at https://doi.org/10.1016/j.jallcom.2025.180516.

Data availability

The data for damage and slip-line detection and stress-strain data from compression and tensile testing is available on zenodo at 10.5281/zenodo.15142966. The data from XRM-Scans is available on zenodo at. 10.5281/zenodo.15144219. Other data will be made available upon reasonable request.

References

[1] J.F. Nie, K.S. Shin, Z.R. Zeng, Microstructure, deformation, and property of wrought magnesium alloys, Met. Mater. Trans. A 51 (12) (2020) 6045–6109, http://dx.doi.org/10.1007/s11661-020-05974-z.

[2] W. Zhang, W. Xiao, F. Wang, C. Ma, Development of heat resistant Mg-Zn-Al-based magnesium alloys by addition of La and Ca: Microstructure and tensile properties, J. Alloys Compd. 684 (2016) 8–14, http://dx.doi.org/10.1016/j.jallcom.2016.05.137.

[3] D. Amberger, P. Eisenlohr, M. Göken, On the importance of a connected hard-phase skeleton for the creep resistance of Mg alloys, Acta Mater. 60 (5) (2012) 2277–2289, http://dx.doi.org/10.1016/j.actamat.2012.01.017.

[4] M. Zubair, S. Sandlöbes-Haut, M.A. Wollenweber, K. Bugelnig, C.F. Kusche, G. Requena, S. Korte-Kerzel, Strain heterogeneity and micro-damage nucleation under tensile stresses in an Mg–5Al–3Ca alloy with an intermetallic skeleton, Mater. Sci. Eng.: A 767 (2019) 138414, http://dx.doi.org/10.1016/j.msea.2019.138414.

[5] M. Zubair, M. Felten, B. Hallstedt, M. Vega Paredes, L. Abdellaoui, R. Bueno Villoro, M. Lipinska-Chwalek, N. Ayeb, H. Springer, J. Mayer, B. Berkels, D. Zander, S. Korte-Kerzel, C. Scheu, S. Zhang, Laves phases in Mg-Al-Ca alloys and their effect on mechanical properties, Mater. Des. 225 (2023) 111470, http://dx.doi.org/10.1016/j.matdes.2022.111470.

[6] M. Masoumi, Q. Zhang, H. Hu, Microstructure and tensile properties of squeeze cast Mg-Al-Ca alloys, Internat. J. Modern Phys. B 23 (6 &7) (2009) 771–776, http://dx.doi.org/10.1142/S0217979209060002.

[7] A.A. Luo, M.P. Balogh, B.R. Powell, Creep and microstructure of magnesium-aluminum-calcium based alloys, Met. Mater. Trans. A 33A (2002) 568–574, http://dx.doi.org/10.1007/s11661-002-0118-1.

[8] T. Homma, S. Nakawaki, S. Kamado, Improvement in creep property of a cast Mg–6Al–3Ca alloy by mn addition, Scr. Mater. 63 (12) (2010) 1173–1176, http://dx.doi.org/10.1016/j.scriptamat.2010.08.033.

[9] B. Kondori, R. Mahmudi, Effect of Ca additions on the microstructure, thermal stability and mechanical properties of a cast AM60 magnesium alloy, Mater. Sci. Eng.: A 527 (7–8) (2010) 2014–2021, http://dx.doi.org/10.1016/j.msea.2009.11.043.

[10] S.W. Xu, N. Matsumoto, K. Yamamoto, S. Kamado, T. Honma, Y. Kojima, High temperature tensile properties of as-cast Mg–Al–Ca alloys, Mater. Sci. Eng.: A 509 (1–2) (2009) 105–110, http://dx.doi.org/10.1016/j.msea.2009.02.024.

[11] A.K. Mondal, A.R. Kesavan, B. Ravi Kiran Reddy, H. Dieringa, S. Kumar, Correlation of microstructure and creep behaviour of MRI230D Mg alloy developed by two different casting technologies, Mater. Sci. Eng.: A 631 (2015) 45–51, http://dx.doi.org/10.1016/j.msea.2015.02.037.

[12] S.M. Zhu, J.F. Nie, B.L. Mordike, Creep and rupture properties of a squeeze-cast Mg-Al-Ca alloy, Met. Mater. Trans. A 37 (4) (2006) 1221–1229, http://dx.doi.org/10.1007/s11661-006-1073-z.

[13] D. Matschkal-Amberger, P. Tuengerthal, S. Lamm, M. Göken, H.W. Höppel, P. Felfer, Understanding the high creep resistance of MRI 230D magnesium alloy through nanoindentation and atom probe tomography, Metals 11 (11) (2021) 1727, http://dx.doi.org/10.3390/met11111727.

[14] L. Han, H. Hu, D.O. Northwood, N. Li, Microstructure and nano-scale mechanical behavior of Mg–Al and Mg–Al–Ca alloys, Mater. Sci. Eng.: A 473 (1–2) (2008) 16–27, http://dx.doi.org/10.1016/j.msea.2007.03.053.

[15] L. Han, D.O. Northwood, X. Nie, H. Hu, The effect of cooling rates on the refinement of microstructure and the nanoscale indentation creep behavior of Mg–Al–Ca alloy, Mater. Sci. Eng.: A 512 (1–2) (2009) 58–66, http://dx.doi.org/10.1016/j.msea.2009.01.068.

[16] L.L. Rohklin, T.V. Dobatkina, N.I. Nikitina, I.E. Tarytina, Calcium-alloyed magnesium alloys, Met. Sci. Heat Treat. 51 (164) (2009) 14–19, http://dx.doi.org/10.1007/s11041-009-9127-7.

[17] R. Ninomiya, T. Ojiro, K. Kubota, Improved heat resistance of Mg-Al alloys by the Ca addition, Acta Met. et Mater. 43 (2) (1995) 669–674, http://dx.doi.org/10.1016/0956-7151(94)00269-N.

[18] M. Zubair, S. Sandlöbes, M.A. Wollenweber, C.F. Kusche, W. Hildebrandt, C. Broeckmann, S. Korte-Kerzel, On the role of laves phases on the mechanical properties of Mg-Al-Ca alloys, Mater. Sci. Eng.: A 756 (2019) 272–283, http://dx.doi.org/10.1016/j.msea.2019.04.048.

[19] M. Zubair, S. Sandlöbes-Haut, M. Lipińska-Chwałek, M.A. Wollenweber, C. Zehnder, J. Mayer, J.-L. Gibson, S. Korte-Kerzel, Co-deformation between the metallic matrix and intermetallic phases in a creep-resistant Mg-3.68Al-3.8Ca alloy, Mater. Des. 210 (2021) 110113, http://dx.doi.org/10.1016/j.matdes.2021.110113.

[20] S. Medghalchi, M. Zubair, E. Karimi, S. Sandlöbes-Haut, U. Kerzel, S. Korte-Kerzel, Determination of the rate dependence of damage formation in metallic-intermetallic Mg–Al–Ca composites at elevated temperature using panoramic image analysis, Adv. Eng. Mater. 25 (21) (2023) http://dx.doi.org/10.1002/adem.202300956.

[21] N. Koundinya, R.S. Kottada, Synergetic influence of microconstituents on the damage accumulation and consequent effect on the flow behaviour in cast Mg–Ca–Sn alloys, Mater. Sci. Eng.: A 799 (2021) 140167, http://dx.doi.org/10.1016/j.msea.2020.140167.

[22] M. Zubair, S. Sandlöbes-Haut, R. Pei, M.A. Wollenweber, L. Berners, C.F. Kusche, C. Liu, F. Roters, J.S.K.-L. Gibson, S. Korte-Kerzel, Strengthening of Mg–Al–Ca alloys with C15 and C36 laves phases, J. Mater. Res. (2023) http://dx.doi.org/10.1557/s43578-023-01082-x.

[23] T.R. Bieler, P. Eisenlohr, C. Zhang, H.J. Phukan, M.A. Crimp, Grain boundaries and interfaces in slip transfer, Curr. Opin. Solid State Mater. Sci. 18 (4) (2014) 212–226, http://dx.doi.org/10.1016/j.cossms.2014.05.003.

[24] A. Tehranchi, M. Lipinska-Chwalek, J. Mayer, J. Neugebauer, T. Hickel, Phase stability and defect studies of mg-based laves phases using defect phase diagrams, 2023, URL http://arxiv.org/pdf/2303.09576v1.

[25] X. Zheng, A.A. Luo, C. Zhang, J. Dong, R.A. Waldo, Directional solidification and microsegregation in a magnesium-aluminum-calcium alloy, Met. Mater. Trans. A 43 (9) (2012) 3239–3248, http://dx.doi.org/10.1007/s11661-012-1159-8.

[26] B. Lu, Y. Li, H. Wang, Y. Wang, W. Yu, Z. Wang, G. Xu, Effects of cooling rates on the solidification behavior, microstructural evolution and mechanical properties of Al–Zn–Mg–Cu alloys, J. Mater. Res. Technol. 22 (2023) 2532–2548, http://dx.doi.org/10.1016/j.jmrt.2022.12.082.

[27] W.-W. Park, B.-S. You, B.-G. Moon, W.-C. Kim, Microstructural change and precipitation hardening in melt–spun Mg–X–Ca alloys, Sci. Technol. Adv. Mater. 2 (1) (2001) 73–78, http://dx.doi.org/10.1016/S1468-6996(01)00028-6.

[28] A. Chu, Y. Zhao, R. Ud-Din, H. Hu, Q. Zhi, Z. Wang, Microstructure and properties of Mg-Al-Ca-Mn alloy with high Ca/Al ratio fabricated by hot extrusion, Mater. (Basel, Switzerland) 14 (18) (2021) http://dx.doi.org/10.3390/ma14185230.

[29] D. Xiao, Z. Chen, X. Wang, M. Zhang, D. Chen, Microstructure, mechanical and creep properties of high Ca/Al ratio Mg-Al-Ca alloy, Mater. Sci. Eng.: A 660 (2016) 166–171, http://dx.doi.org/10.1016/j.msea.2016.03.001.

[30] B. Jing, S. Yangshan, X. Feng, X. Shan, Q. Jing, T. Weijian, Effect of extrusion on microstructures, and mechanical and creep properties of Mg–Al–Sr and Mg–Al–Sr–Ca alloys, Scr. Mater. 55 (12) (2006) 1163–1166, http://dx.doi.org/10.1016/j.scriptamat.2006.08.020.

[31] Z.T. Li, X.G. Qiao, C. Xu, X.Q. Liu, S. Kamado, M.Y. Zheng, Enhanced strength by precipitate modification in wrought Mg–Al–Ca alloy with trace Mn addition, J. Alloys Compd. 836 (2020) 154689, http://dx.doi.org/10.1016/j.jallcom.2020.154689.

[32] Z. Nasiri, M. Sarkari Khorrami, H. Mirzadeh, M. Emamy, Enhanced mechanical properties of as-cast Mg-Al-Ca magnesium alloys by friction stir processing, Mater. Lett. 296 (2021) 129880, http://dx.doi.org/10.1016/j.matlet.2021.129880.

[33] Y. Nakaura, A. Watanabe, K. Ohori, Effects of Ca,Sr additions on properties of Mg-Al based alloys, Mater. Trans. 47 (4) (2006) 1031–1039.

[34] W.J. Delis, P.C. Huckfeldt, B. Hallstedt, P.-L. Sun, D. Raabe, S. Korte-Kerzel, S. Sandlöbes-Haut, Influence of Al and Ca on the ductility of Mg–Al–Ca alloys, Adv. Eng. Mater. (2023) http://dx.doi.org/10.1002/adem.202301071.

[35] S. Sandlöbes, M. Friák, S. Korte-Kerzel, Z. Pei, J. Neugebauer, D. Raabe, A rare-earth free magnesium alloy with improved intrinsic ductility, Sci. Rep. 7 (1) (2017) 10458, http://dx.doi.org/10.1038/s41598-017-10384-0.

[36] M. Everingham, L. van Gool, C.K.I. Williams, J. Winn, A. Zisserman, The pascal visual object classes (VOC) challenge, Int. J. Comput. Vis. 88 (2) (2010) 303–338, http://dx.doi.org/10.1007/s11263-009-0275-4.

[37] S. van der Walt, J.L. Schönberger, J. Nunez-Iglesias, F. Boulogne, J.D. Warner, N. Yager, E. Gouillart, T. Yu, the scikit-image contributors, Scikit-image: image processing in python, PeerJ 2 (2014) e453, http://dx.doi.org/10.7717/peerj.453.

[38] W.E. Lorensen, H.E. Cline, Marching cubes: A high resolution 3D surface construction algorithm, ComputerGraphics 21 (4) (1987) 163–169, http://dx.doi.org/10.1145/37402.37422.

[39] S. Pang, G. Wu, W. Liu, M. Sun, Y. Zhang, Z. Liu, W. Ding, Effect of cooling rate on the microstructure and mechanical properties of sand-casting Mg–10Gd–3Y–0.5Zr magnesium alloy, Mater. Sci. Eng.: A 562 (2013) 152–160, http://dx.doi.org/10.1016/j.msea.2012.11.016.

[40] S. Amerioun, S.I. Simak, U. Häussermann, Laves-phase structural changes in the system CaAl2-xMgx, Inorg. Chem. 42 (5) (2003) 1467–1474, http://dx.doi.org/10.1021/ic020596m.

[41] A. Suzuki, N.D. Saddock, J.W. Jones, T.M. Pollock, Solidification paths and eutectic intermetallic phases in Mg–Al–Ca ternary alloys, Acta Mater. 53 (9) (2005) 2823–2834, http://dx.doi.org/10.1016/j.actamat.2005.03.001.

[42] A.A. Griffith, G.I. Taylor, VI. The phenomena of rupture and flow in solids, Philos. Trans. R. Soc. Lond. Ser. A, Contain. Pap. Math. Phys. Character 221 (582–593) (1921) 163–198, http://dx.doi.org/10.1098/rsta.1921.0006.

[43] M. Freund, D. Andre, P.L. Sun, C.F. Kusche, S. Sandlöbes-Haut, H. Springer, S. Korte-Kerzel, Plasticity of the C15-CaAl2 laves phase at room temperature, Mater. Des. 225 (2023) 111504, http://dx.doi.org/10.1016/j.matdes.2022.111504.

[44] S. Korte-Kerzel, Microcompression of brittle and anisotropic crystals: recent advances and current challenges in studying plasticity in hard materials, MRS Commun. 7 (2) (2017) 109–120, http://dx.doi.org/10.1557/mrc.2017.15.

[45] F. Stein, A. Leineweber, Laves phases: a review of their functional and structural applications and an improved fundamental understanding of stability and properties, J. Mater. Sci. 56 (9) (2021) 5321–5427, http://dx.doi.org/10.1007/s10853-020-05509-2.

[46] M. Freund, Z. Xie, P.-L. Sun, L. Berners, J. Spille, H. Wang, C. Thomas, M. Feuerbacher, M. Lipinska-Chwalek, J. Mayer, S. Korte-Kerzel, Influence of chemical composition on the room temperature plasticity of C15 Ca-Al-Mg Laves phases, Acta Mater. 276 (2024) 120124, http://dx.doi.org/10.1016/j.actamat.2024.120124.

[47] S. Schröders, S. Sandlöbes, C. Birke, M. Loeck, L. Peters, C. Tromas, S. Korte-Kerzel, Room temperature deformation in the Fe7Mo6 μ -phase, Int. J. Plast. 108 (2018) 125–143, http://dx.doi.org/10.1016/j.ijplas.2018.05.002.

[48] J. Guénolé, M. Zubair, S. Roy, Z. Xie, M. Lipińska-Chwałek, S. Sandlöbes-Haut, S. Korte-Kerzel, Exploring the transfer of plasticity across laves phase interfaces in a dual phase magnesium alloy, Mater. Des. 202 (2021) 109572, http://dx.doi.org/10.1016/j.matdes.2021.109572.

[49] A. Tireira, G. Requena, S. Sao Jao, A. Borbely, H. Klocker, Rupture of intermetallic networks and strain localization in cast AlSi12Ni alloy: 2D and 3D characterization, Acta Mater. 112 (2016) 162–170, http://dx.doi.org/10.1016/j.actamat.2016.04.020.

[50] K. Bugelnig, H. Germann, T. Steffens, F. Sket, J. Adrien, E. Maire, E. Boller, G. Requena, Revealing the effect of local connectivity of rigid phases during deformation at high temperature of cast AlSi12Cu4Ni(2,3)Mg alloys, Mater. (Basel, Switzerland) 11 (8) (2018) http://dx.doi.org/10.3390/ma11081300.

[51] S. Sanyal, M. Paliwal, T.K. Bandyopadhyay, S. Mandal, Evolution of microstructure, phases and mechanical properties in lean as-cast Mg–Al–Ca–Mn alloys under the influence of a wide range of Ca/Al ratio, Mater. Sci. Eng.: A 800 (2021) 140322, http://dx.doi.org/10.1016/j.msea.2020.140322, URL https://www.sciencedirect.com/science/article/pii/S0921509320313861.

[52] K.V. Yang, C.H. Cáceres, A.V. Nagasekhar, M.A. Easton, The skin effect and the yielding behavior of cold chamber high pressure die cast Mg–Al alloys, Mater. Sci. Eng.: A 542 (2012) 49–55, http://dx.doi.org/10.1016/j.msea.2012.02.029.

Further reading

[1] S. Medghalchi, E. Karimi, S.-H. Lee, B. Berkels, U. Kerzel, S. Korte-Kerzel, Three-dimensional characterisation of deformation-induced damage in dual phase steel using deep learning, Mater. Des. 232 (2023) 112108, http://dx.doi.org/10.1016/j.matdes.2023.112108.